AFRL-RB-WP-TR-2011-3117

STRUCTURAL TECHNOLOGY EVALUATION AND ANALYSIS PROGRAM (STEAP)
Delivery Order 0045: Progressive Failure Analysis of Translaminar Reinforced Composite Structures

Padmasiri Vipul Ranatunga

Miami University

NOVEMBER 2011
Final Report

AIR FORCE RESEARCH LABORATORY
AIR VEHICLES DIRECTORATE
WRIGHT-PATTERSON AIR FORCE BASE, OH 45433-7542
AIR FORCE MATERIEL COMMAND
UNITED STATES AIR FORCE

NOTICE AND SIGNATURE PAGE

Using Government drawings, specifications, or other data included in this document for any purpose other than Government procurement does not in any way obligate the U.S. Government. The fact that the Government formulated or supplied the drawings, specifications, or other data does not license the holder or any other person or corporation; or convey any rights or permission to manufacture, use, or sell any patented invention that may relate to them.

This report was cleared for public release by the USAF 88th Air Base Wing (88 ABW) Public Affairs (AFRL/PA) Office and is available to the general public, including foreign nationals. Copies may be obtained from the Defense Technical Information Center (DTIC) (http://www.dtic.mil).

AFRL-RB-WP-TR-2011-3117 HAS BEEN REVIEWED AND IS APPROVED FOR PUBLICATION IN ACCORDANCE WITH ASSIGNED DISTRIBUTION STATEMENT.

//SIGNED//

STEPHEN B. CLAY, Ph.D.
Program Manager
Analytical Structural Mechanics Branch
Structures Division

//SIGNED//

MICHAEL J. SHEPARD, Ph.D.
Chief
Analytical Structural Mechanics Branch
Structures Division

//SIGNED//

DAVID M. PRATT, Ph.D.
Technical Advisor
Structures Division
Air Vehicles Directorate

This report is published in the interest of scientific and technical information exchange, and its publication does not constitute the Government's approval or disapproval of its ideas or findings.

*Disseminated copies will show "//signature//" stamped or typed above the signature blocks.

REPORT DOCUMENTATION PAGE

Form Approved
OMB No. 0704-0188

1. REPORT DATE *(DD-MM-YY)*	2. REPORT TYPE	3. DATES COVERED *(From - To)*
November 2011	Final	05 February 2010 – 13 January 2012

4. TITLE AND SUBTITLE
STRUCTURAL TECHNOLOGY EVALUATION AND ANALYSIS PROGRAM (STEAP)
Delivery Order 0045: Progressive Failure Analysis of Translaminar Reinforced Composite Structures

5a. CONTRACT NUMBER
FA8650-04-D-3446-0045

5b. GRANT NUMBER

5c. PROGRAM ELEMENT NUMBER
62201F

6. AUTHOR(S)
Padmasiri Vipul Ranatunga

5d. PROJECT NUMBER
2401

5e. TASK NUMBER
N/A

5f. WORK UNIT NUMBER
A0HD0B

7. PERFORMING ORGANIZATION NAME(S) AND ADDRESS(ES)
By: Miami University
Middletown, OH 45066
For: General Dynamics Information Technology
5100 Springfield Pike, Suite 509
Dayton, OH 45431

8. PERFORMING ORGANIZATION REPORT NUMBER
AFRL-RB-WP-TR-2011-3117

9. SPONSORING/MONITORING AGENCY NAME(S) AND ADDRESS(ES)
Air Force Research Laboratory
Air Vehicles Directorate
Wright-Patterson Air Force Base, OH 45433-7542
Air Force Materiel Command
United States Air Force

10. SPONSORING/MONITORING AGENCY ACRONYM(S)
AFRL/RBSM

11. SPONSORING/MONITORING AGENCY REPORT NUMBER(S)
AFRL-RB-WP-TR-2011-3117

12. DISTRIBUTION/AVAILABILITY STATEMENT
Approved for public release; distribution unlimited.

13. SUPPLEMENTARY NOTES
PAO case number 88ABW-2012-0727, cleared 10 Feb 2012. Report contains color.

14. ABSTRACT
This task is to develop and implement advanced finite element analysis methods for predicting the response of damaged composite aircraft structures with and without z-pins.

15. SUBJECT TERMS
traction-separation based analysis of z-pinned composites, end notched flexure (ENF), double cantilever beam (DCB)

16. SECURITY CLASSIFICATION OF:			17. LIMITATION OF ABSTRACT:	18. NUMBER OF PAGES	19a. NAME OF RESPONSIBLE PERSON (Monitor)
a. REPORT	b. ABSTRACT	c. THIS PAGE			Stephen Clay
Unclassified	Unclassified	Unclassified	SAR	34	19b. TELEPHONE NUMBER *(Include Area Code)* N/A

Table of Contents

List of Figures

List of Tables

Preface

This technical report covers the work performed from February 4, 2010 to January 13, 2012 under United States Air Force Contract FA8650-04-D-3446, Delivery Order 45: "Progressive Failure Analysis of Translaminar Reinforced Composite Structures".

This contract was administered under the technical direction of Dr. Stephen Clay, AFRL/RBSM, Air Vehicles Directorate, Air Force Research Laboratory (AFRL), Wright-Patterson Air Force Base (WPAFB), Ohio, 45433-6533.

General Dynamics Information Technology, 5100 Springfield Pike, Suite 509, Dayton, OH 45431, served as the prime contractor, and Mr. Kevin Hunt was the senior contract administrator. Miami University, 501 E. High Street; 102 Roudebush Hall, Oxford, OH 45056, served as the subcontractor, and Dr. Vipul Ranatunga was the Principal Investigator.

1. SUMMARY

Composite materials are becoming a popular material of choice for recent and upcoming military aircraft structure. These materials perform well when loaded in-plane, but out-of-plane loads often cause delaminations. As more composite materials are inserted into the fleet, the designers and maintainers need to be able to accurately predict the damage growth as a function of service loads. Current state-of-the-art analysis methods fall short, especially in the area of predicting the behavior of translaminar reinforced composites. Therefore, an extensive evaluation of the current state-of-the-art modeling techniques has been conducted to understand the strengths and weaknesses of the existing techniques.

The report has been divided into two chapters based on the two main objectives of the research project. Each section provides the details of the numerical methods, experimental procedures, and the relevant conclusions and future work. Summary of the work performed to achieve these two objectives are given below.

1.1 Damage Growth under Mode-I Loading in Z-Pinned Composites

Traction-separation based cohesive modeling approach has been developed to predict the effect of z-pinning on laminated composites. As a result of this study, experimental characterization of the frictional effect due to z-pinning has been completed. Numerical simulation of the progressive damage due to delaminations between plies with and without z-pinning has been simulated and compared with experimental results. Complete details of the experimental investigations using double cantilever beam (DCB) tests with and without z-pinning are documented in Chapter 2. The frictional effect due to the presence of z-pins has been incorporated within the finite element model. A traction-separation law and a cohesive-zone model have been developed to model the delamination. The finite element model captured the overall response of the DCB samples under Mode-I loading consistently. The approach presented in this work does not capture the details of the damage due to matrix cracking and fiber breakage taking place at the interface and elsewhere.

1.2 Testing and Analysis of Delamination under Mode-II Loading

Procedures for the determination of Mode-I fracture energy using the double cantilever beam test has been well document and standardized. There has been progress in recent years towards standardizing Mode-II delamination using the end-notched flexure (ENF) test. Under Chapter 3 of this report, the testing of the End Notched Flexure (ENF) specimen to determine the fracture energy of laminated composites under Mode-II loading is presented. Using the guidelines and suggestions in the published literature, detailed experimental investigation has been completed to assess the suitability of the proposed ENF testing for the determination of Mode-II fracture toughness. In Chapter 3, results from the numerical simulations have been compared against the experimental observations. Difficulties inherent to Mode-II testing of composite delamination are discussed in detail, and the remedies suggested in the published literature are reiterated to overcome these challenges.

2. Damage Growth Under Mode-I Loading in Z-Pinned Composites

Summary: Z-Pinning has been used effectively for improving the delamination resistance of laminated composite structures. The pin density, diameter and length are some of the parameters related to the effectiveness of z-pins for increasing the delamination resistance. Phenomenological as well as physics-based modeling approaches have been proposed in the past to evaluate the effectiveness of z-pinning and predict the load-bearing capacity of z-pinned composite structures. Recent developments with finite element based modeling techniques have introduced numerous design tools to model damage and predict the remaining useful life of composite structures. During the current work, a traction-separation based cohesive modeling approach was developed to predict the effect of z-pinning on laminated composites. During this study, a detailed characterization of traction-separation laws to represent the frictional effect due to z-pinning was performed. Utilizing these experimental results, numerical simulation of the progressive damage due to delaminations between plies with and without z-pinning has been simulated and compared with experimental results. Details of the experimental results using double cantilever beam (DCB) tests with and without z-pinning are presented for IM7/977-3 graphite/epoxy. The modeling approach taken in this study utilizing the cohesive elements within the Abaqus® finite element software has proven that the models can predict the behavior of z-pinned composites close to experimental observations.

2.1 Introduction

Simulation of delamination in laminated composites has received considerable attention in recent years due to increased use of composite materials in aerospace and related industries. Mainly in the context of finite element analyses, the goal has been to capture not only the onset (initiation) of delamination, but also the progression. Towards this end, the Virtual Crack Closure Technique [1, 2] (VCCT) enables the extraction of mode-specific strain energy release rates at a crack tip within a finite element framework to evaluate if a delamination-type crack will extend. Using the nodal forces at the crack-front and the displacements behind the crack-front, strain energy release rates can be calculated in a finite element analysis to predict self-similar crack growth. As an alternative to fracture mechanics based VCCT, interface models, widely known as cohesive models [3, 4] have become a widely used tool for modeling damage, particularly delamination-type crack growth. Cohesive models are more convenient to implement within a finite element framework, do not require pre-existing cracks, hence enabling the prediction of crack initiation as well as propagation. Both of these state-of-the-art methods have been incorporated into various general purpose finite element software packages [5].

Composite materials have been used in aerospace applications to reduce the weight as well as improve the functionality of the structure by tailoring the strength properties. Delamination between plies in laminated composite structures has proven to be one of the major challenges in utilizing composite materials in various applications. Design strategies and effective utilization of laminated composite materials for composite structures rely on the capabilities of predicting the interlaminar failure under various loading and environmental conditions. Both VCCT and cohesive element approaches have been utilized effectively in predicting the interlaminar failure under various loading conditions.

Two methods of reinforcing composite laminates through the thickness of the part are z-pinning and stitching [6-8]. Both of these techniques have been successfully transitioned to aerospace applications, but only in a limited number of applications. Several researchers have developed analytical and numerical modeling methods to predict the behavior of z-pinned and stitched composites [9-11]. Most of these methods are limited to a selected set of boundary and loading conditions limiting their application. These approaches are implemented as numerical procedures within certain finite element packages as add-on tools or extended functionalities.

The approach presented in this chapter utilizes the cohesive element technique as implemented in the Abaqus® finite element software to model the effect of z-pinning on delamination failure of composite materials under Mode-I type loading. Detailed characterization of the frictional effect of z-pins is presented under Section 2.2 based on the flatwise tension (FWT) tests performed with IM7/977-3 graphite/epoxy. Traction-separation laws required for cohesive modeling, derived from these experiments are presented under Section 2.3, followed by the finite element model used to simulate Mode-I type delamination with the presence of z-pins. Comparison of results between FEA simulations and experimental data is given under Section 2.4, followed by conclusions and future work.

2.2 Experimental Details

2.2.1 Flatwise Tension Tests

To characterize the frictional behavior of z-pins under tensile loading, FWT tests were performed per ASTM Standard D7291/D7291M – 07 [12]. Square panels were fabricated from IM7/977-3 unidirectional prepeg with a layup of [0_{12}, Teflon, 0_{12}]. The Teflon film was used to prevent bonding between the top and bottom halves. Z-pins were inserted through the entire 24-ply stack in a grid pattern, with each square grid containing 3 x 3, 6 x 6, or an entire area covered with z-pins as shown in Figure 2.1. The z-pins used in this study were pultruded rods made from carbon fiber and BMI resin. Two different panels were made with 2% and 4% pin densities and 0.51 mm (0.02") pin diameter. After curing these panels in an autoclave, square blocks were machined out of the panels (see Figure 2.2) and glued with Hysol® 9430 two part epoxy resin to T-shaped test fixtures, as shown in Figure 2.3. Each specimen was tested under displacement control with an MTS Alliance RT/10 system.

The specimens were loaded until all of the pins were completely pulled out of the top or bottom half. The crosshead displacement versus force was recorded for each specimen. Compliance calibration of this test setup was performed by gluing the two T-shaped fixtures together without the composite specimen (see Figure 2.4) and pulling them beyond the maximum load observed during the z-pin pullout tests. The measured crosshead displacement for each specimen was modified to reflect the deformation of the test setup.

After testing, the quality of each sample was assessed based on the straightness of the driven z-pins. It is difficult to evaluate the angle of z-pins before pulling them apart. It was observed that the likelihood of having ill-driven pins increases with a smaller number of z-pins. Additionally, certain z-pinned areas were not centered on the square-blocks which created a bending effect during testing. The results of these off-centered samples were discarded. It was also seen that some specimens experienced excessive bending during testing which may cause the z-pins to break prematurely. The results from these samples were also discarded.

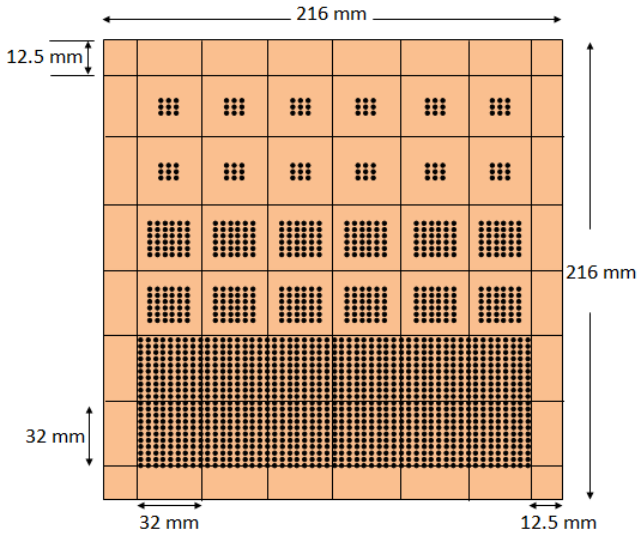

Figure 2.1 Z-Pin Layout for FWT Samples

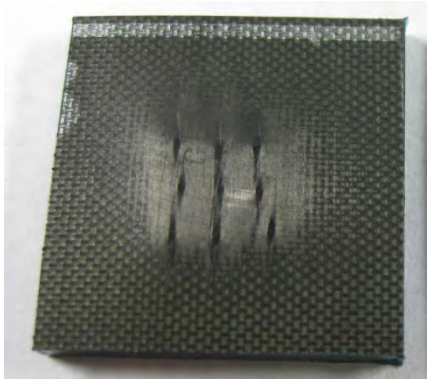

Figure 2.2 Z-Pinned Sample Used for FWT

Figure 2.3 FWT Test Fixture with a Sample Glued

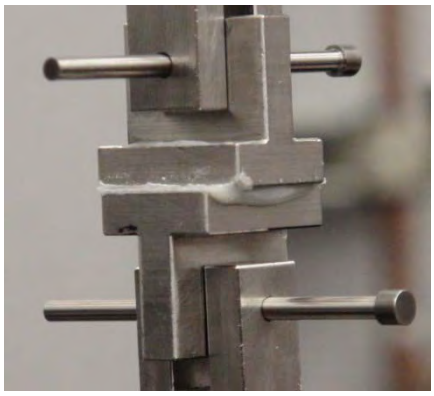

Figure 2.4 Compliance Calibration for FWT Test

For this study, the most important parameter to obtain from the FWT tests is the debond strength of the z-pins. This information can be derived from the maximum load measured during the test. Table 2.1 displays the measured loads achieved, as well as the calculated value of load per pin. The values for all of the samples were very consistent, even across the different pin densities. The average load per pin for 2% density was found to be 68 N, while the average load per pin for 4% was 71 N. The overall average maximum load per pin for both densities was found to be 70 N with a standard deviation of 10 N.

Table 2.1 Maximum Load in FWT Tests

# Pins	Max Load (N)	Max Load/Pin (N)
9	510	57
9	506	56
9	541	60
36	2522	70
36	2953	82
36	3031	84
	Avg	**68**
	St Dev	**13**

(a) 2% Aerial Density

# Pins	Max Load (N)	Max Load/Pin (N)
9	590	66
9	771	86
9	637	71
9	616	68
36	2402	67
36	3137	87
36	2714	75
36	2560	71
36	2532	70
121	6481	54
110	6744	61
	Avg	**71**
	St Dev	**9.7**

(b) 4% Aerial Density

2.2.2 Double Cantilever Beam Tests

A series of double cantilever beam (DCB) tests were performed to determine the effectiveness of z-pins at improving the delamination resistance of composite laminates. Unidirectional IM7/977-3 carbon/epoxy laminae were hand laid-up and co-cured in the zero degree direction to create double cantilever beam specimens. A 0.0127 mm thick Teflon film was placed at the mid-plane to create an initial crack length of 51 mm as shown in Figure 2.5. No adhesive was used between the two composite laminae. To avoid fiber bridging, $\pm 3^0$ plies were used at the mid-plane [13, 14]. A region of unreinforced co-cured composite extended 32 mm from the initial crack tip. A 51 mm long z-pin field was inserted into the DCB specimen after the co-cured region. The z-pins used in this study were pultruded rods made from carbon fiber and BMI resin. Similar to FWT tests, 0.51 mm diameter z-pins were chosen with 2% aerial density.

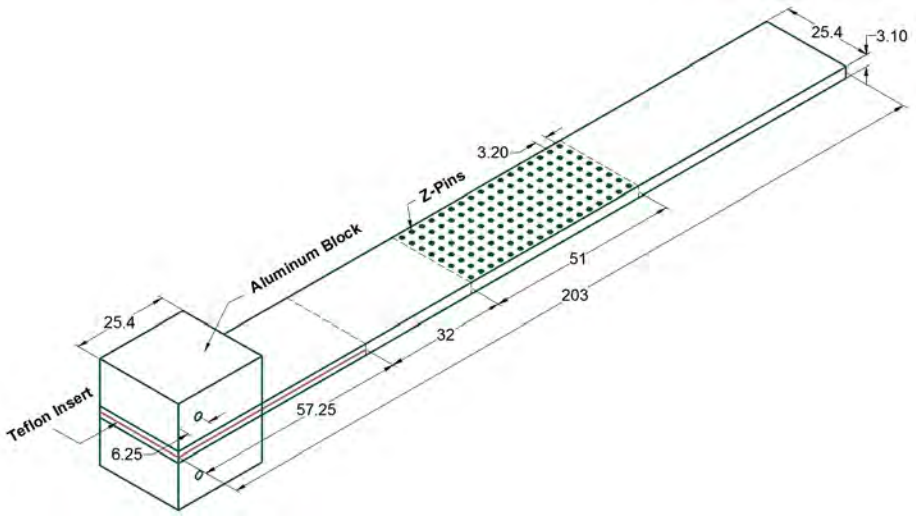

Figure 2.5 Schematic of Double Cantilever Beam Specimen

As a result of the z-pin insertion process, excess foam material and the protruding part of the z-pin must be trimmed off. The trimming process applies a significant side force on the z-pin field, pushing the pins to an inclined angle. In order to hold the z-pins perpendicular to the panel during trimming, the pins were driven through a rubber sheet that was placed on top of the laminate as shown in Figure 2.6. Based on previous work by Clay et.al [8], commercial strength Neoprene was found to be able to resist the heat of the curing process without leaving any residue on the panel. The z-pin field produced as a result of this procedure is shown in Figure 2.7. This process produced a considerably straight z-pin field compared to the trials without a supporting rubber sheet.

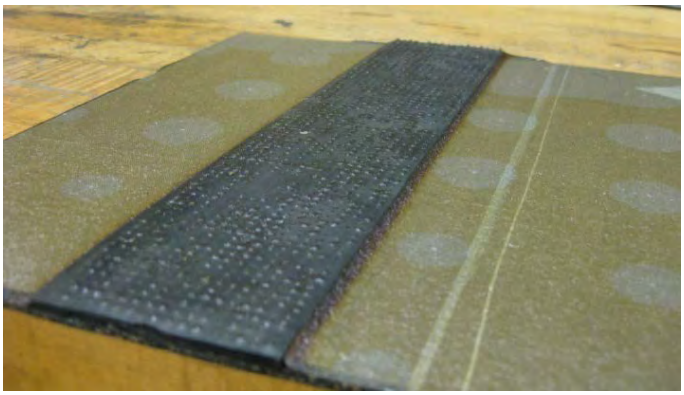

Figure 2.6 Rubber Sheet used to Support Z-Pins

Figure 2.7 Z-Pin Field After the Removal of Rubber Sheet

The standard test method ASTM D 5528 [15] was followed. The DCB specimens were attached to the load frame with the loading block technique as shown in Figure 2.8. A constant displacement rate of 1 mm/min was used during each test. It is necessary to identify the fracture energy corresponding to each z-pin row as the crack grows through the z-pin field along the beam. In order to trace the failure of each z-pin row, the location of each row was marked along the side of the DCB specimen (see Figure 2.9). A special camera arrangement was set up to take snapshots of the row marks at five second intervals.

Figure 2.8 DCB Specimen in Pin-Loaded Fixture

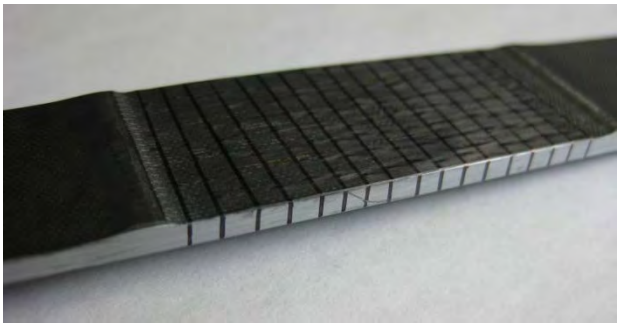

Figure 2.9 Rows of Z-Pins Marked Along the Side of the Beam

Figure 2.10 displays the crack-opening images that correspond to the load drops on the load-displacement curve for a DCB specimen with 2% pin density. The numbers on the graph and images correspond to the number of z-pin row. For example, the 9-15 on the load-displacement plot represents a simultaneous failure of z-pin row 9 through z-pin row 15. The side-by-side images were taken immediately before and immediately after the load drop during the DCB test.

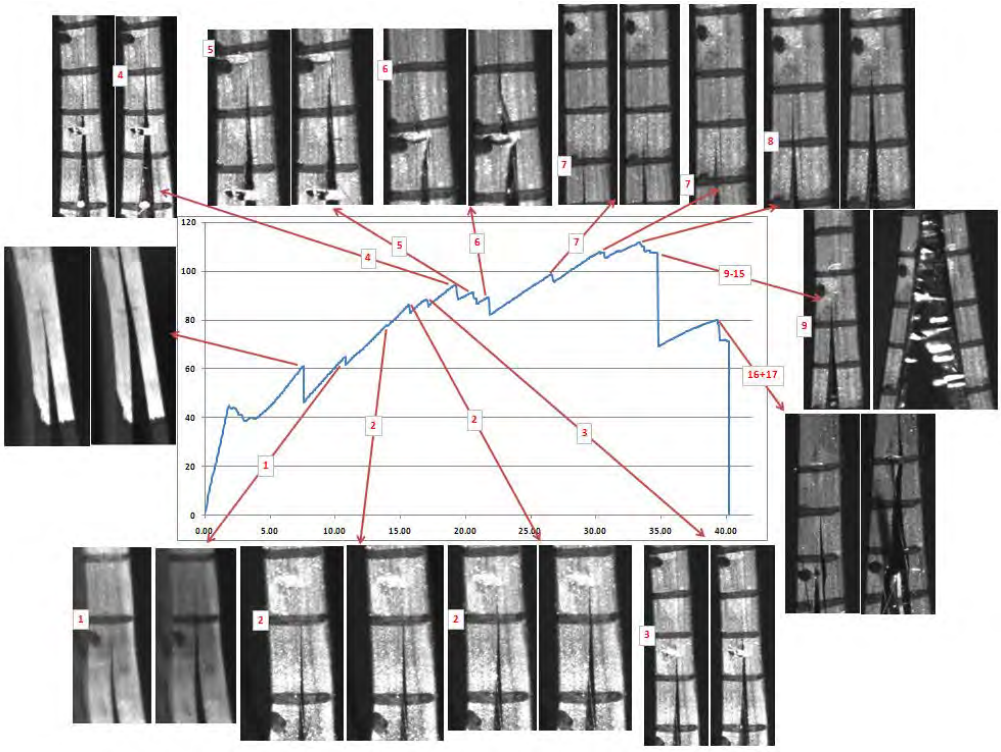

Figure 2.10 Load-Displacement Curve for DCB Displaying Z-Pin Pullout and Corresponding Load-Drop

Following the tests, the critical energy release rates for initiation and propagation were determined with a modified beam theory [16]. Table 2.2 shows both the elastic and fracture properties of IM7/977-3 which were obtained from experimental results and from the open literature.

Table 2.2 Elastic and Fracture Properties of IM7/977-3

E_1 (MPa)	E_2 (MPa)	E_3 (MPa)	G_{12} (MPa)	G_{13} (MPa)	G_{23} (MPa)
158,000	8,644	8,644	4,660	4,660	3,600
ν_{12}	$\nu_{23} = \nu_{13}$	G_{IC} (KJ/m^2)	G_{IIC} (KJ/m^2)	G_{IIIC} (KJ/m^2)	η
0.316	0.012	0.218	0.753	0.753	1.8

2.3 Numerical Modeling

The damage process of laminated composites consists of both interlaminar damage due to delamination and intralaminar damage mechanisms such as matrix cracking and fiber fracture. During this study, only the interlaminar damage due to delamination has been considered, and a finite element model has been developed to study the effect of z-pins on resisting delamination. Traction-separation based cohesive approach has been taken to model the delamination between plies, as well as frictional effect due to the presence of z-pins. A brief outline of cohesive modeling, including the parameters that are needed to model with cohesive elements available in commercial software Abaqus® is highlighted in the following section.

2.3.1 Cohesive Zone Modeling

Cohesive zone models were introduced by Barenblatt [3] and Dugdale [4] for modeling elastic-plastic fracture in ductile metals, extended further by Hillerborg et al. [17] for modeling quasi-brittle materials. Cohesive models have been used successfully over the last few decades to study fracture when the crack path is known in advance. The geometry is discretized into elements and the prospective crack-path or multiple crack-paths are aligned with element boundaries and the interface between the prospective crack path is modeled by inserting the cohesive elements to predict initiation and propagation of progressive damage along the crack path. Figure 2.11 shows a commonly used traction-separation law where σ_{db} is the debonding strength of the material, and G_c is the the area under the curve representing fracture energy of the material. Additionally, the cohesive model introduces an artificial elastic modulus E_n, producing elastic deformation prior to the initiation of damage, which has to be avoided by introducing a relatively high dummy stiffness for interface elements, which is not a material-related parameter. Debond strength and fracture energy for a given material can be determined by experiments. As an example, using a DCB test, debonding value and fracture energy corresponding to Mode-I type crack propagation can be determined. Selecting an arbitrarily soft value for E_n may introduce a considerable compliance to the interface, while a higher stiffness may cause spurious traction oscillations [18].

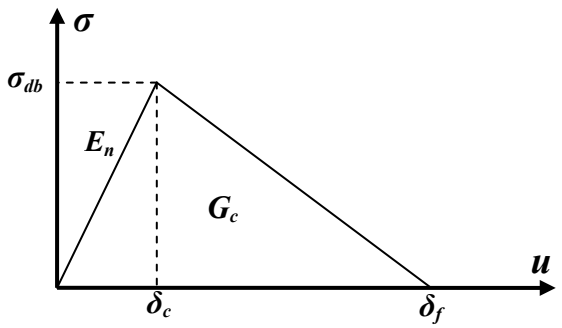

Figure 2.11 Traction-Separation Law used to Define Cohesive Model and the related Parameters

The idea of a *fracture process zone*, and a cohesive-zone to represent the failure taking place in ductile metals, has been adapted to represent the degrading mechanism in composite failure. Lumping together all the different failure mechanisms taking place at the crack-tip, such as microcracking and coalescence of the matrix material, debonding between fiber and matrix, etc., a cohesive zone model is defined using a stress-displacement relationship. Effect of z-pinning

can also be defined with a cohesive law to reflect the overall behaviour of the composite under a given loading condition. In this study, cohesive elements in ABAQUS® finite element software package are used to model debonding under Mode-I loading. Two separate cohesive zones (traction-separation laws) have been defined with a number of parameters including interfacial penalty stiffness, interfacial debond strength, and the critical fracture energy, to represent the delamination between plies with and without z-pinning. A detailed description of the finite element model is given under the next section.

2.3.2 Finite Element Modeling Approach

Consider the layup of z-pins as shown in Figure 2.12 where the initial crack with Teflon insert and the z-pin layup is shown in (a); the mid-plane of the double cantilever beam with equivalent surface areas representing z-pins is shown in (b); and the 2D representation used for the finite element simulations is shown in (c). Areas of interest for the finite element model can be categorized as the initially unbonded area where the Teflon is inserted, delaminated area before reaching the z-pins, area with z-pins, and the area in between two rows of z-pins.

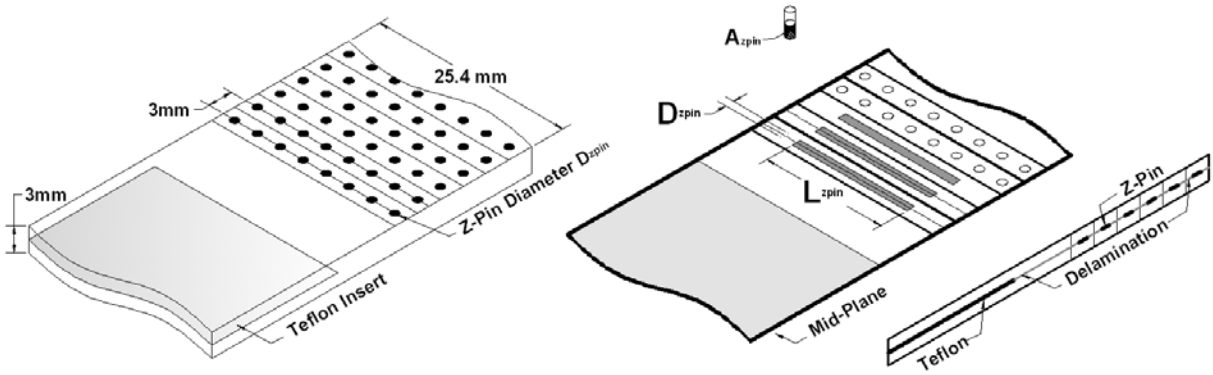

(a). Z-Pin layup (b). Mid-plane and (c). 2D representation

Figure 2.12 Identification of area occupied by z-pins and the representative areas.

A section of the finite element mesh highlighting the separate delamination areas used to represent z-pins, delamination before z-pins, and the delamination between two rows of z-pins, are shown in Figure 2.13.

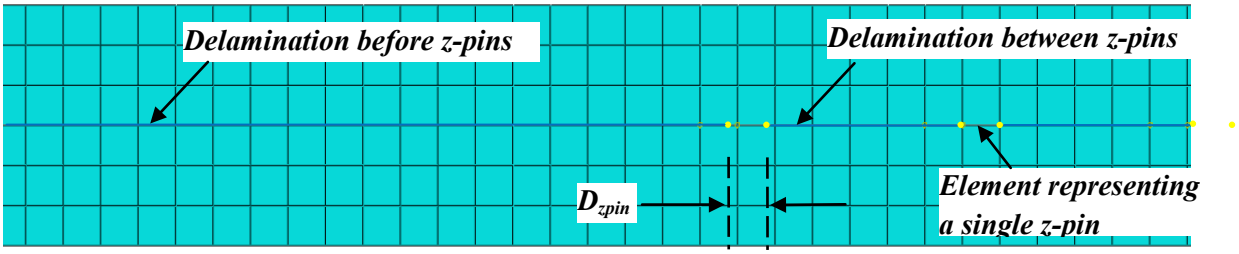

Figure 2.13 Two dimensional representation of bonded areas used in FEA simulations.

In this finite element model, the frictional resistance between the z-pins and the resin was represented by an area equivalent to the embedded cylindrical surface area of the z-pins above or

below the mid-plane as shown in Figure 2.12 (b). In order to represent all the pins in any given row of z-pins, a rectangular area equal to D_{zpin} x L_{zpin} in the width direction was used in a 2D plane-strain finite element model as shown in Figure 2.12 (c) where,

$$L_{zpin} = (A_{zpin} \text{ x Number of pins in a row})/ D_{zpin} \quad (2.1)$$

2.3.3 Estimation of Debond Strength for the Cohesive Zone Model

Two separate cohesive models were used to represent the delamination in the areas without z-pins (delamination before the z-pin area and the delamination between z-pin rows), and the delamination in each row of z-pins. It is necessary to have a correct estimate for the debonding strength in order to accurately predict the initiation of damage. For the areas without z-pins, an estimated debonding value of 15 MPa was found based on the finite element simulations with cohesive elements. In addition to cohesive zone models, a VCCT model can also be used to simulate delamination and this approach requires only the critical energy release rate (G_c) to simulate delamination. Comparison between VCCT and cohesive results for various debond strength values are shown in Figure 2.14 (a). When compared with experimental results, debond strength of 15 MPa produced comparable results for the portion of delamination without z-pins as shown in Figure 2.14 (b).

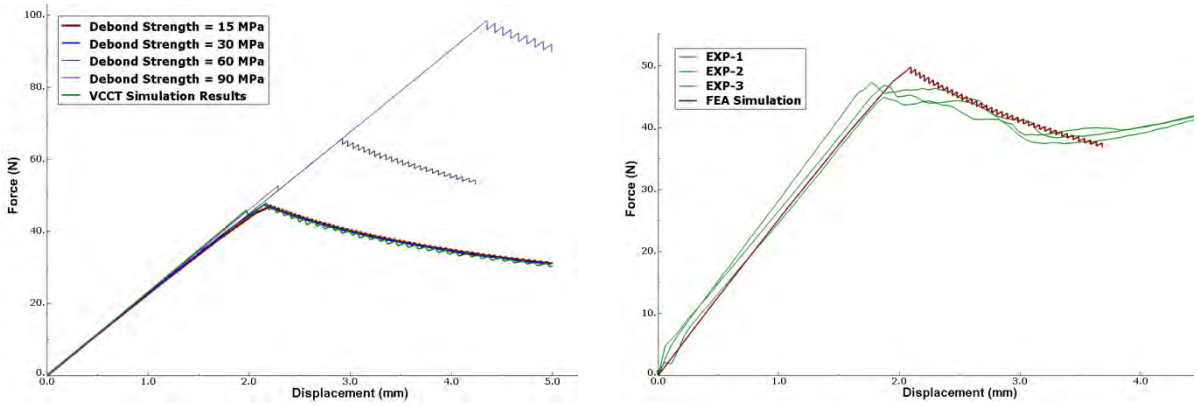

(a) FEA Simulation Results **(b) FEA Model and Experimental Results**

Figure 2.14 Reaction Force vs Displacement with Different Debond Strengths for Delamination

For the area with z-pins, debond strength σ_{db} for the cohesive law is calculated based on the average load observed during the FWT tests reported under the Section 2.21. A constant frictional shear stress on the z-pin surface area can be calculated based on the FWT tests, and use this as the debonding strength for each z-pin on the cohesive zone model. The debond strength can be expressed as

$$\sigma_{db} = P_{average}/(\pi.D_{zpin}.L_e) \quad (2.2)$$

where, $P_{average}$ is the average load observed under Section 2.2.1, and L_e is the half of the embedded pin-length. For the cases with 2% pin density and 0.51 mm diameter z-pins, L_e was

observed as 1.45mm, and $P_{average}$ is reported as 70 N under Section 2.2.1, hence the debond strength σ_{db} is found to be 30 N/mm^2. For illustration purposes, different values of debond strength for z-pins and the corresponding reaction forces predicted by the model are shown in Figure 2.15.

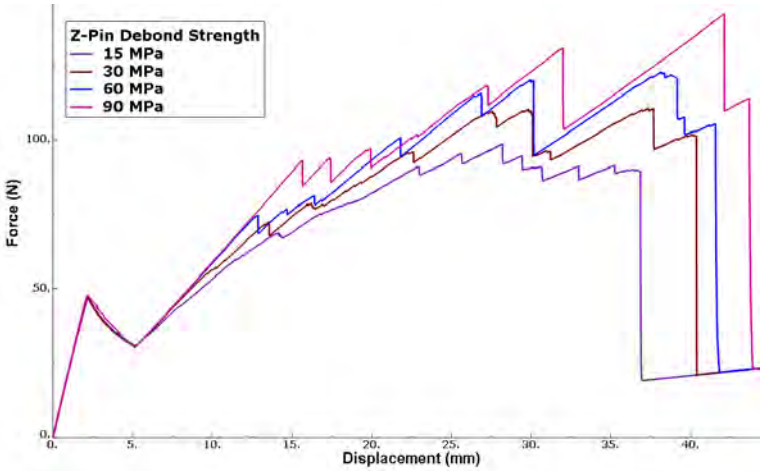

Figure 2.15 Reaction Force vs Displacement for Different Debond Strengths of Z-Pins

For the initial delamination without z-pins, a debond strength of 15 MPa was used with all these simulations based on the results shin in Figure 2.14. According to the results shown in Figure 2.15, simulation of z-pin pullout can be affected considerably without a proper estimate of the debond strength.

2.3.4 Estimation of Fracture Energy for Each Row of Z-Pins

In order to model the debonding with a cohesive zone model, the second important material parameter is the fracture energy, as explained under Section 2.3.1. Due to the presence of z-pins (acting like fiber-bridging), fracture energy increases with the crack length producing a fracture resistance curve as shown in Figure 2.16. Therefore, in order to recognize the fracture energy associated with each row of z-pins, resistance curve has been divided into segments based on the z-pin pullout observed during the experiments (see Figure 2.10). The highlighted areas under the resistance curve in Figure 2.16 correspond to the *total fracture energy* associated with each row of z-pins. But, in order to represent the fracture energy associated with each row of z-pins in the finite element model, it is necessary to produce the fracture energy per unit area (G_c). Since a 2D plain strain finite element model is used for the simulations, Gc was calculated by dividing this polygonal area associated with each z-pin row by the diameter of the z-pins.

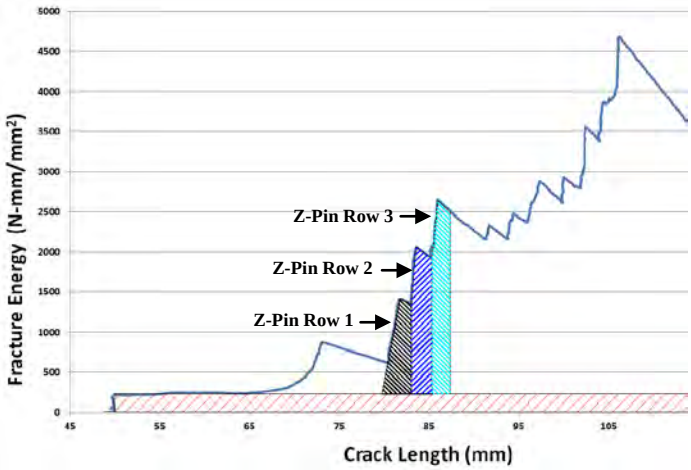

Figure 2.16 Fracture Energy vs Crack Length for a Z-Pinned Sample

2.4 Results and Discussion

With the help of the FWT and the DCB tests, appropriate values for the debond strength and the fracture energy to represent the z-pins under Mode-I delamination were determined. Using these experimentally determined values, finite element simulations have been conducted to predict the behavior of the composite delamination under Mode-I loading. Comparison of the finite element results against three DCB tests are shown in Figure 2.17. According to these results, finite element model could capture the overall behavior closely. The discrepancy at the initial region before reaching the first row of z-pins is due to a hump on the DCB samples as a result of a rubber sheet used for z-pinning (see Figure 2.6).

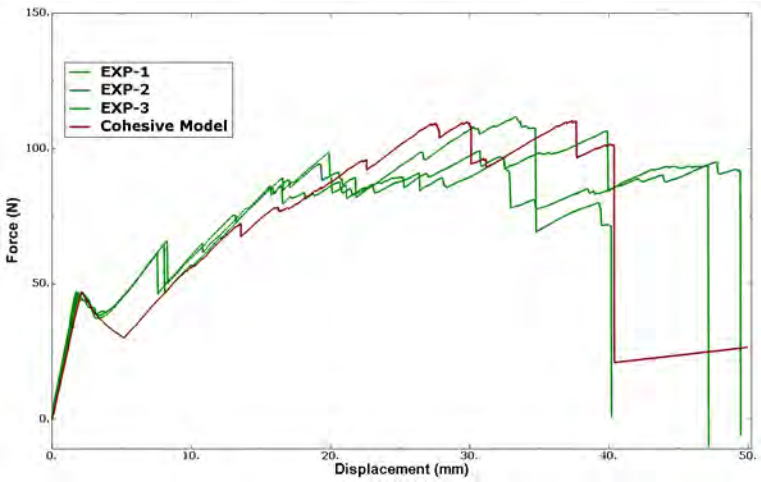

Figure 2.17 Comparison of Results Predicted by FEA Against Experimental Data

This finite element model can be used to study the effects of embedded z-pin length and the pin-diameter, provided that the corresponding resistance curve and the associated fracture energies for each z-pin are provided for the model. Furthermore, with the spacing of the z-pins appropriately in the finite element model, the effect of z-pin density on the delamination resistance can also be studied.

2.5 References

1. Rybicki, E. F., Kanninen, M. F., "A finite element calculation of stress intensity factors by a modified crack closure integral", *Engineering Fracture Mechanics*, Vol. 9, 1977, pp. 931-938.
2. Raju, I. S., "Calculation of strain energy release rates with higher order and singular elements", *Engineering Fracture Mechanics*, Vol. 28, 1987, pp. 251-274.
3. Barenblatt, G. I., "The formation of equilibrium cracks during brittle fracture - general ideas and hypothesis, axially symmetric cracks", *Prikl. Math. Mekh*., Vol. 23, No. 3, 1959, pp. 434-444.
4. Dugdale, D. S., "Yielding of steel sheets containing slits", *Journal of the Mechanics and Physics of Solids*, Vol. 8, 1960, pp. 100-104.
5. Dassault Systemes Simulia Corp., *Abaqus Analysis User's Manual*, Providence, RI, 2011.
6. Dickinson LC, Farley GL, Hinders MK, "Translaminar reinforced composites: A review," *Journal of Composites Technology and Research,* Vol. 21, No. 1, 1999, pp. 3-15.
7. Freitas G, Magee C, Dardzinski P, Fusco T, "Fiber insertion process for improved damage tolerance in aircraft laminates," *Journal of Advanced Materials,* Vol. 25, No. 4, 1994, pp. 36-43.
8. Clay S. B, Pommer A. K, Jones R. P, " Novel two-step ultrasonic approach for reinforcing co-bonded composite joints using z-fiber™ stubble", *AIAA/ASME/ASCE/AHS/ASC Structures, Structural Dynamics and Materials Conf* erence, 2005, pp. 7026-7042.
9. Grassi, M. and Zhang, X., "Finite Element Analyses of Mode I Interlaminar Delamination in Z-fibre Reinforced Composite Laminates," *Comp. Sci. and Tech.*, Vol. 63, 2003, pp. 1815-1832.
10. Cartie', D. R., Dell'Anno, G., Poulin, E., and Partridge, I. K., "3D Reinforcement of stiffener-to-skin T-joints by Z-pinning and Tufting," *Engineering Fracture Mechanics*, Vol. 73, 2006, pp. 2532-2540.
11. Yan, W., Liu, H-Y, and Mai, Y-W, "Numerical Study on the Mode I Delamination Toughness of Z-pinned Laminates," Comp. Sci. and Tech., Vol. 63, pp. 1481-1493, 2003.
12. ASTM Standard D7291 / D7291M - 07 Standard Test Method for Through-Thickness "Flatwise" Tensile Strength and Elastic Modulus of a Fiber-Reinforced Polymer Matrix Composite Material, ASTM International, West Conshohocken, PA, 2007, DOI: 10.1520/D7291_D7291M-07, www.astm.org.
13. Johnson, W. S, Mangalgiri, P. D., "Investigation of fiber bridging in double cantilever beam specimens", *Journal of Composites Technology and Research*, Vol. 9, No. 1, 1987, pp. 10-13.

14. O'Brien, T. K, Martin, R. H., "Round robin testing for Mode I interlaminar fracture toughness of composite materials", " *Journal of Comp. Tech. and Research*, Vol. 15, No. 4, 1993, pp.269-281.

15. ASTM Standard D5528-01, "Standard test method for Mode I Interlaminar Fracture Toughness of Unidirectional Fiber-Reinforced Polymer Matrix Composites," ASTM International, West Conshohocken, PA, 2007, DOI: 10.1520/D5528-94A, www.astm.org.

16. Dransfield, K. A., Jain, L. K., and Mai, Y. W. , "On the effects of stitching in CFRPs – I. Mode I delamination toughness," *Composites Science and Technology,* Vol. 58, 1998, pp. 815-827.

17. Hillerborg, A., Modeer, M., Petersson, P.E., "Analysis of crack formation and crack growth in concrete by means of fracture mechanics and finite elements", *Cement Concrete Research*, Vol. 6, 1976, pp. 773–782.

18. Schellekens, J. J, de Borst, R., "On the numerical integration of interface elements", International Journal of Numerical Methods in Engineering, Vol. 36, 1992, pp. 43–66.

3. Testing and Analysis of Delamination under Mode-II Loading

Summary: Testing of the End Notched Flexure (ENF) specimen to determine the fracture energy of laminated composites under Mode-II loading is presented under this part of the report. Experiments have been conducted following the guidelines and suggestions in the published literature. Difficulties inherent to Mode-II testing of composite delamination are discussed in detail, and the remedies suggested in the published literature are reiterated to overcome these challenges. Results from the numerical simulations have been compared against the experimental observations.

3.1 Introduction

The design of damage tolerant composite structures requires an in-depth understanding of crack growth under various loading conditions. In order to simplify the complex loading conditions that exist in everyday use of these composite structures, crack growth is studied under various idealized loading conditions such as Mode I, Mode II, or Mode III, and well-defined combinations of these idealized modes. One of the primary means of crack propagation in laminated composites is interlaminar delamination, which has been studied widely under these idealized modes of loading. Procedures for the determination of Mode-I fracture energy using the double cantilever beam test has been well document and standardized. There has been progress in recent years towards standardizing Mode-II delamination using the end-notched flexure (ENF) test [1]. Davidson et al. [2] have made recommendations for test geometry and data reduction methods to be used with unidirectional fiber reinforced polymeric composites. Based on these studies as well as further studies by Davidson et al. [3, 4], the American Society for Testing and Materials (ASTM) committee D30 has recently decided to use the ENF test as the standard test method for determining Mode-II fracture toughness.

This study is concerned with the determination of Mode-II fracture toughness based on the guidelines presented by Davidson et el. [1] and compares the results against numerical predictions with finite element based Virtual Crack Closure Technique (VCCT). Based on the previous work by Davidson [5], it has been suggested that the maximum load point to be used in the calculation of fracture toughness. The current investigation reveals that a considerable difference exists between the fracture toughness calculated based on the nonlinear load point versus the maximum load point. Difficulties associated with observing the correct crack-initiation and locating the crack tip after damage are discussed in this chapter. Significant difference observed in fracture energy calculated using the pre-cracked and non-pre-cracked samples is also presented.

3.2 Experimental Details

ENF specimens were fabricated with 48 zero-degree plies of IM7/977-3 graphite epoxy prepreg tape. Each specimen was 254 mm long, having an average width of 25.4 mm, and an average height of 6.28 mm. An initial crack length was created by placing a 0.013 mm thick sheet of Teflon along the mid-plane. Material properties obtained by tensile testing of the samples from the same batch are given in Table 3.1.

Table 3.1 Material data for unidirectional IM7/977-3 graphite epoxy

E_1 (MPa)	$E_2 = E_3$ (MPa)	$G_{12} = G_{13}$ (MPa)	G_{23} (MPa)	$\nu_{12} = \nu_{13}$	ν_{23}
156,000	8,198	4,750	4,953	0.32	0.65

Based on the specifications given by Davidson et al. [1] for the sample geometry, a 102 mm span of the specimen was chosen as the supported length between the rollers. The distance between the crack-tip and the left-roller was adjusted for compliance calibration (CC) and cracking, as shown in Figure 3.1. Compliance calibration of the test specimen was conducted by placing the crack-tip 40 mm (CC-1) and 20 mm (CC-2) from the left support roller. The three-point bend setup as shown in Figure 3.2 is used for this experiment. In order to closely monitor the crack initiation and to measure the distances accurately, a traveling optical microscope was used.

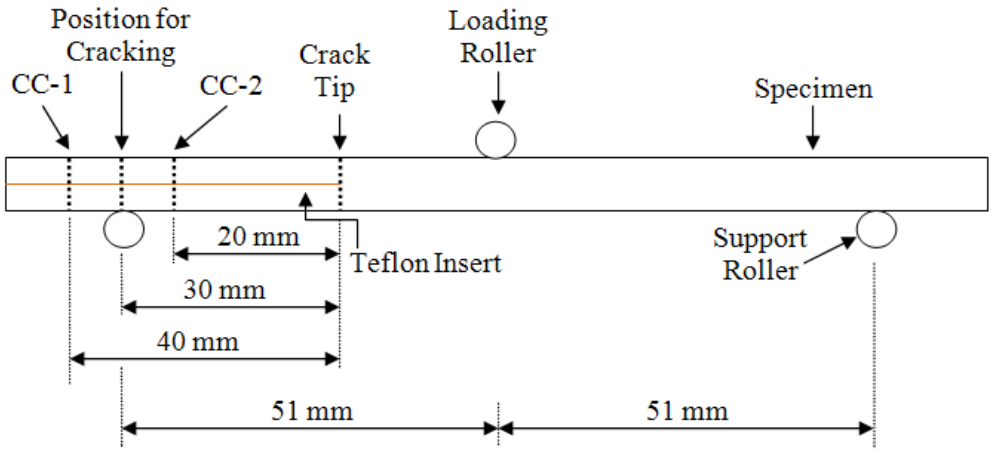

Figure 3.1 Specimen geometry and position marks for the compliance-calibration and cracking

For each crack length used in the CC test, the specimen was loaded up to 50% of the failure load predicted by [1]

$$P_c = \frac{4B}{3a}\left[G_{IIC}\, E_{1f}\, h^3\right]^{1/2} \qquad (3.1)$$

where, B is the specimen width, a is the crack length (20 mm or 40 mm), G_{IIC} is the best-known Mode-II fracture energy, E_{1f} is the flexural modulus, and $2h$ is the specimen thickness. The specimen was placed on the fixture and loaded at a rate of 0.1 mm/min under displacement control for compliance calibration at 20 mm and 40 mm. After the two compliance calibrations, the specimen was repositioned so that the crack tip was 30 mm from the left roller and was loaded under displacement control until the load reached the peak value and subsequently started dropping with the advancement of the crack front. A plot of crosshead displacement versus load

data as shown in Figure 3.3 was used to determine the compliance coefficients. Least squares linear regression was used to determine the compliance coefficients, avoiding the initial nonlinear portions of these curves.

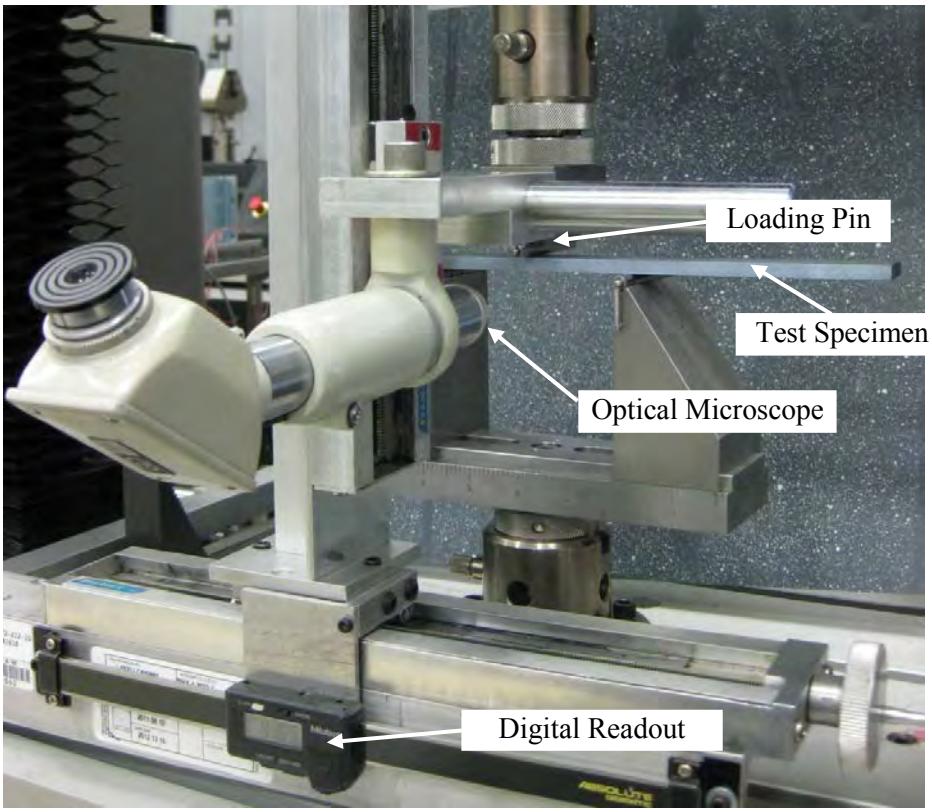

Figure 3.2. Experimental setup for end-notched flexure test

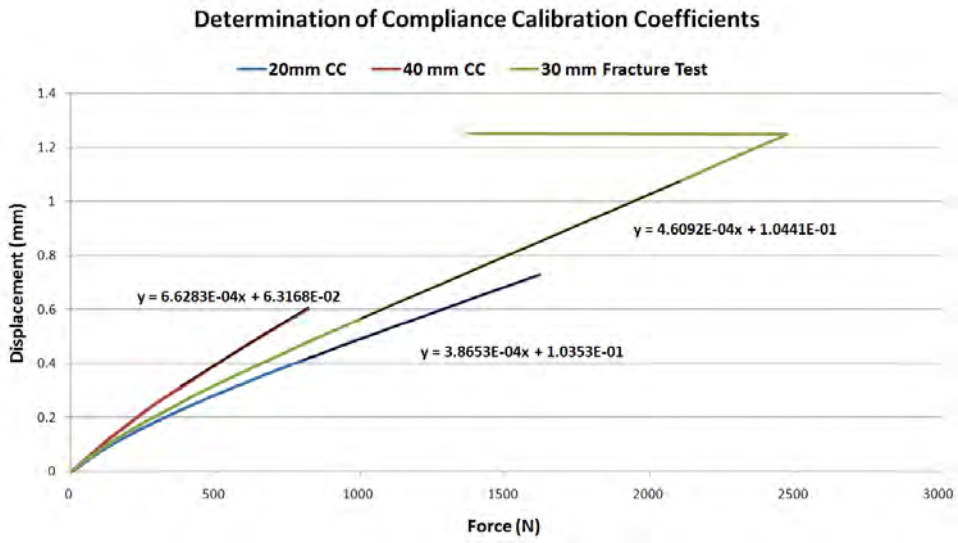

Figure 3.3. Compliance calibration and fracture data for an ENF sample

Once the compliances were determined, a plot of the compliance coefficients versus the crack-length cubed was generated [1] as shown in Figure 3.4 and a least squares linear regression analysis was used to determine the slope (m) and the intercept (A) of the plotted data. As an example, the sample data shown in Figure 3.4 has a slope of 5.0055 x 10^{-9} and an intercept of 3.3824 x 10^{-4} and the compliance C can be expressed as

$$C = A + m\,a^3 = 3.3824 \times 10^{-4} + (5.0055 \times 10^{-9})\,a^3 \quad (3.2)$$

According to Linear Elastic Fracture Mechanics (LEFM), the strain energy release rate is defined as

$$G = \frac{P^2}{2}\frac{\delta C}{\delta a} \quad (3.3)$$

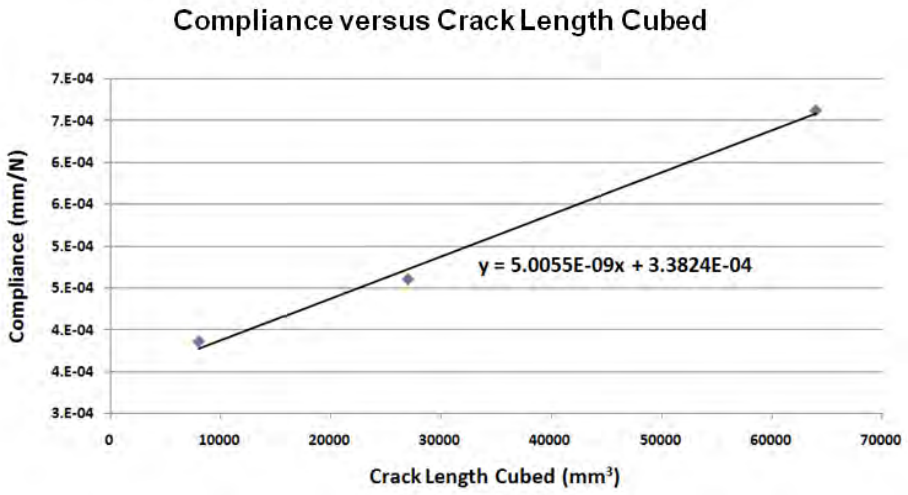

Figure 3.4. Plot of crack length versus crack length cubed to determine the slope (m) and intercept (A).

Considering the ENF specimen geometry and the compliance expressed in Eq. 3.2, the fracture toughness of the material can be determined using

$$G_{IIC} = \frac{3mP_c^2\,a_c^2}{2B} \quad (3.4)$$

where, m is the slope determined above, a_c is the crack length (30 mm), and P_c is the peak load observed during the test.

If a clear display of nonlinearity was displayed before reaching the peak load, the fracture toughness for crack-initiation could be determined using the value of the load corresponding to the initiation of the nonlinear load point. As shown in Figure 3.5, the precracked samples displayed a nonlinear load point corresponding to the crack initiation when observed carefully through the traveling optical microscope.

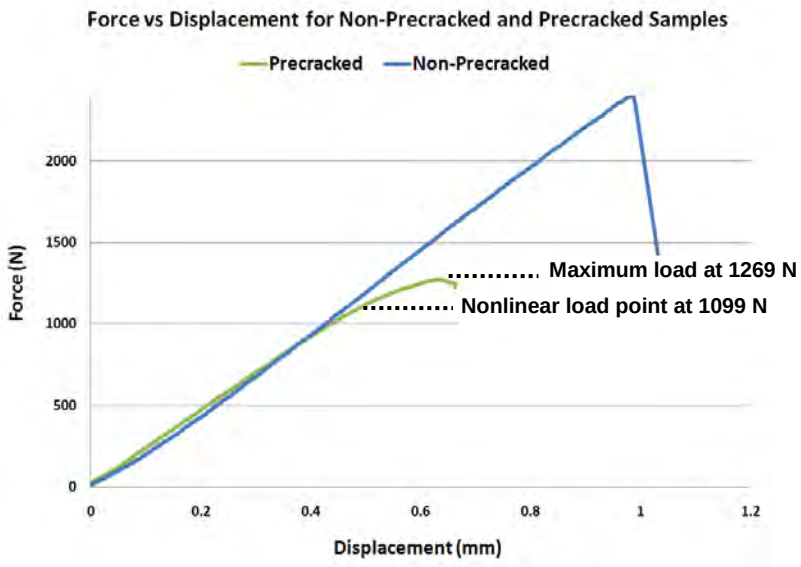

Figure 3.5. Stable crack growth in precracked sample, displaying a significant difference between nonlinear load point and maximum load.

With the non-precracked samples, the nature of the crack propagation was sudden, displaying only a peak point on the load versus crosshead displacement plot. Therefore, the maximum fracture toughness was calculated using the peak load observed during the fracture tests for both the precracked and non-precracked samples. The fracture energy associated with crack initiation was calculated for the precracked samples based on the nonlinear load point observed on Figure 3.5.

The location of the new crack tip was observed in the vicinity of the middle loading roller, but varied widely between different samples. Davidson et al. [1] has proposed an approach to calculate the current crack tip based on the compliance of the unloading curve using

$$a_{calc} = \left[\frac{m_u - m}{A}\right]^{1/3} \tag{3.5}$$

where m and A are the coefficients determined previously for Eq. 3.2 using the non-precracked compliance calibrations and m_u is the compliance of the unloading curve.

When the load dropped suddenly due to the advancement of the crack front, the machine started unloading at a rate of 0.6 mm/min and recorded the unloading data. As this process takes place, an observer had adequate time to visually examine and locate the current crack tip since the crack tip had a better visibility when it was loaded. The traveling optical microscope was aligned with the new crack tip and the distance from the left roller (in Figure 3.1) to the newly formed crack tip was measured for comparison with the calculated value based on Eq. 3.5.

3.3 Numerical Modeling

The damage process of laminated composites consists of both interlaminar damage due to delamination and intralaminar damage mechanisms such as matrix cracking and fiber fracture. During this study, only the interlaminar damage due to delamination has been considered, and a finite element model has been developed to study the delamination under Mode-II loading. The VCCT approach readily available in the Abaqus® finite element software package is used during this study, and a brief outline of this technique is given in the following section.

3.3.1 Virtual Crack Closure Technique (VCCT)

The Virtual Crack Closure Technique [6, 7] enables the extraction of mode-specific stain energy release rates at a crack tip within a finite element framework to evaluate if a delamination-type crack will extend. Using the nodal forces at the crack-front and the displacements behind the crack-front, strain energy release rates can be calculated in a finite element analysis to predict self-similar crack growth. The Virtual Crack Closure Technique uses the principle of Linear Elastic Fracture Mechanics (LEFM) to predict the crack propagation taking place along a predefined surface. VCCT assumes that the strain energy released during a crack extension is the same energy required to close the crack.

3.3.2 Finite Element Modeling Approach

Material properties listed in Table 3.1 and the Mode-II fracture energy determined with the ENF test can be used to predict the behavior of an ENF under displacement control. A two-dimensional model of an ENF with corresponding loading and boundary conditions is shown in Figure 3.6. The reaction force predicted by the finite element model at the point where the displacement is applied can be used to compare against the measured force of the testing machine.

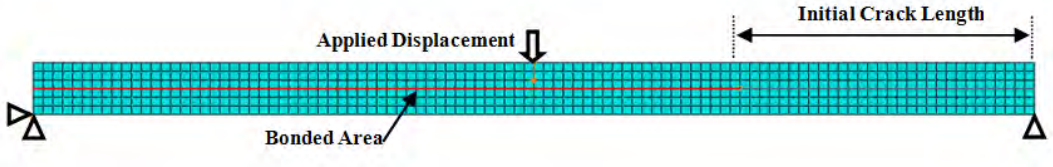

Figure 3.6. Finite element model with boundary and loading conditions

3.4 Results

The end notched flexure test procedure described in the previous section has been used to find the Mode-II fracture toughness of IM7/977-3 graphite epoxy. Four undamaged specimens were tested to find the non-precracked fracture toughness. These specimens were further tested to find the fracture toughness of the precracked specimens. Certain samples needed manual cracking to create a straight and perpendicular crack front in the direction of crack advancement. A sharp wedge was driven between the two sub-plies (see Figure 3.7) to open the crack front until a balanced crack length was observed from both sides of the specimen. Even though the crack length was balanced by observing the crack-tip on each side of the test specimen, the profile of the crack was not observed experimentally to verify the straightness of the crack front.

The experimentally determined fracture energy of the non-precracked samples in Table 3.2 displayed a significantly higher value compared to the precracked samples in Table 3.3.

Additionally, the fracture energy is considerably different when the peak load point versus nonlinear load-point data is used for calculations.

The reaction force measured at the middle roller in the experimental setup (see Figure 3.1) is plotted against the compliance-calibrated displacement in Figure 3.8. In the same plot, the reaction force predicted by the finite element model at the middle of the specimen in Figure 3.6 is plotted against the applied displacement. The average fracture energy reported in Table 3.2 is used for the finite element simulation. According to the comparisons in Figure 3.8, the finite element model with fracture energy of 1519 J/m^2 over-predicted the peak reaction force. In comparison with the experimental results, the fracture energy was decreased until a better match was reached. It was found that fracture energy of 1000 J/m^2 produced comparable finite element results.

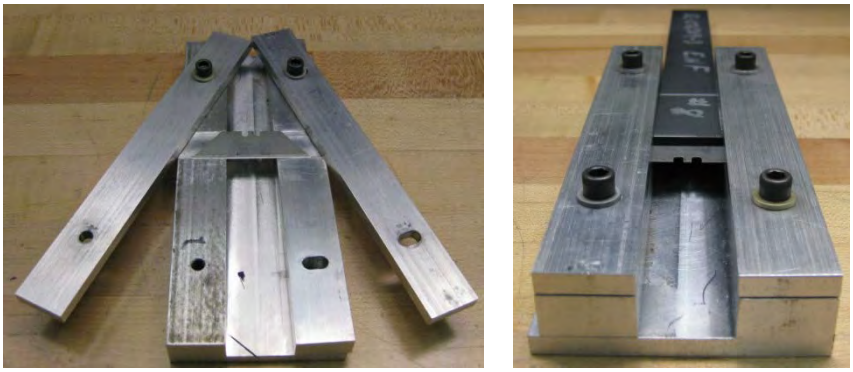

Figure 3.7. Sharp wedge used to open the crack front

Table 3.2 Fracture toughness for non-precracked specimens

NPC	P_{peak} (N)	$G_{c,max}$ (J/m^2)
1	2404	1569
2	2471	1701
3	2259	1287
Average		1519
Std. Dev.		212

Table 3.3 Fracture toughness for precracked specimens

PC	$P_{nonlinear}$ (N)	$G_{C,\ init}$ (J/m^2)	P_{peak} (N)	$G_{C,\ max}$ (J/m^2)
1-PC1	1296	437	1391	503
1-PC2	1094	311	1222	388
1-PC3	1099	314	1269	419
1-PC4	1148	343	1320	453
2-PC1	1039	281	1293	435
3-PC1	1182	363	1320	453
3-PC2	1066	296	1326	457
Average		335		444
Std. Dev.		53		36

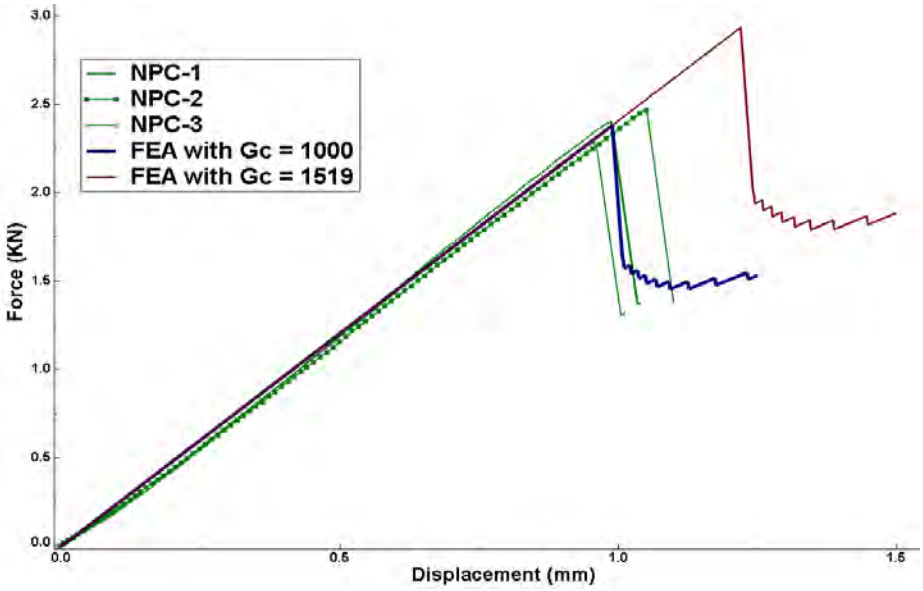

Figure 3.8. Comparison of experimental results against finite element simulations

3.5 References

1. Davidson, B.D., S.S. Teller. 2010. "Recommendations for an ASTM standardized test for determining G_{IIC} of unidirectional laminated polymeric matrix composites", *Journal of ASTM International*, 7(2): 1-11.

2. Davidson, B.D., X. Sun. 2006. "Geometry and data reduction recommendations for a standardized end notched flexure test for unidirectional composites", *Journal of ASTM International*, 3(9): 1-19.

3. Davidson, B.D., X. Sun. 2005. "Effect of friction, geometry, and fixture compliance on the perceived toughness from three and four point bend end notched flexure tests", *Journal of Reinforced Plastics*, 24(15): 1611-1628.

4. Davidson, B.D., X. Sun, A.J. Vinciquerra. 2007. "Influences of friction, geometric nonlinearity, and fixture compliance on three and four point bend end notched flexure test results", *Journal of Composite Materials*, 41(10): 1177-1196.

5. Davidson, B.D. "Towards an ASTM standardized test for determining G_{IIC} of unidirectional laminated polymeric matrix composites", presented at the 21st Annual American Society for Composites Technical Conference, September 17-20, 2006.

6. Rybicki, E. F., M. F. Kanninen. 1997. "A finite element calculation of stress intensity factors by a modified crack closure integral", *Engineering Fracture Mechanics*, 9: 931-938.
7. Raju, I. S. 1987. "Calculation of strain energy release rates with higher order and singular elements", *Engineering Fracture Mechanics*, 28: 251-274.
8. Benzeggagh, M. L., M. Kenane. 1996. "Measurement of Mixed-mode Delamination Fracture Toughness of Unidirectional Glass/epoxy Composites with Mixed-mode Bending Apparatus," *Composite Science and Technology*, 56(4): 439-449.

4. CONCLUSIONS

An efficient and simplistic approach has been presented under Chapter 2 for modeling the effect of z-pinning on delamination under Mode-I type loading. The approach proposed in this chapter utilizes existing modeling techniques within the Abaqus® finite element software package. The overall response of the DCB samples under Mode-I loading has been captured consistently if the crack resistance curve is discretized along the z-pin field. If the average fracture energy is used for all the z-pins, the predicted load carrying capacity is much higher, over-estimating the strength under Mode-I loading.

The simplistic approach presented with the cohesive model is not capable of capturing the fine details of the damage taking place at the interface and elsewhere. Once the delamination resistance is increased with z-pinning, other damage mechanisms such as ply cracking, fiber breakage, and matrix microcracking may take place due to significant bending of the arms of the DCB specimen. During this study, only the delamination and z-pin debonding under Mode-I is considered. Additionally, the simplified 2D finite element model assumed a simultaneous pullout of all the pins in any given row of z-pins in the through-width direction. This may not happen in practice due to the z-pin angle, misalignment of z-pins in a given row, and the difference in bonding between the pins and laminates. These discrepancies have been observed during experimental trials and it may be the root cause of large scatter of measured force towards the end of the z-pin field.

Only the delamination of z-pinned composites under Mode-I loading is studied in this research. This work will be continued with the experimental characterization and numerical modeling of delamination under Mode-II loading with z-pins. Additionally, the finite element approach has to be developed to a level in which the model could be used as a predictive tool, assessing the delamination resistance at different pin densities, diameters, and depths and predicting these under mixed-mode loading conditions. Geometrically complicated structural components will be studied under mixed-mode loading conditions to assess the capabilities of the proposed approach in predicting the structural response with z-pinning.

Testing of the ENF specimen to determine the fracture energy of laminated composites under Mode-II loading is presented under Chapter 3 of the report. Difficulties inherent to Mode-II testing of composite delamination are discussed in detail. It has been observed that when the non-precracked samples are used for ENF testing, it is difficult to locate the exact location of the crack-front. Teflon insert may shift during the fabrication and autoclave processes, even though the location is marked during the layup process. Therefore, advanced techniques such as ultrasonic c- scans are necessary to locate the crack front accurately. Visual inspections with an optical microscope may not be accurate enough to locate the exact crack front under Mode-II loading since the crack between two sub-plies will not open similar to Mode-I loading. Therefore, an over estimation of the crack length may have produced a higher value for the fracture energy. In the case of the precracked specimens, a sharp wedge was inserted to open the sub-plies slightly (without forcing the crack to propagate further) and the tip was located using an optical microscope. Both sides of the specimen were inspected to make sure that the crack front was balanced, but the profile of the crack inside the specimen was unknown. This may create undesirable results, producing very low calculated values for fracture energy.

Based on the results from preliminary investigations, it was observed that the calculated crack location is considerably smaller compared to the visually measured crack length. Further

investigations are necessary to understand the difference and make corrections to the experimental procedure to predict the crack length accurately. Only the two sides of the specimen were observed during the visual inspections and the profile of the crack front was unknown. Therefore, an accurate estimation of the crack location is required for validation of the calculation procedure.

LIST OF ACRONYMS, ABBREVIATIONS, AND SYMBOLS

ASTM	American Society for Testing and Materials
CC	Compliance Calibration
DCB	Double Cantilever Beam
ENT	End Notched Flexure
FEA	Finite Element Analysis
FWT	Flatwise Tension
LEFM	Linear Elastic Fracture Mechanics
MTS	Materials Testing Systems
VCCT	Virtual Crack Closure Technique

A	Intercept
a_c	Crack Length
a_{calc}	Calculated Crack Length
A_{zpin}	Embedded Area of the Z-Pin
D_{zpin}	Diameter of the Z-Pin
E_{1f}	Flexural Modulus
E_n	Artificial Elastic Modulus
G_c	Fracture Toughness
L_e	Half-Embedded Pin Length
L_{zpin}	Embedded Length of the Z-Pin
m	Gradient
$P_{average}$	Average Load
P_c	Critical (or peak) Load
δ_c	Critical Separation
δ_f	Separation at Complete Failure
σ_{db}	Debond Strength